C. R. Mecanique 345 (2017) 248–258

Contents lists available at ScienceDirect

Comptes Rendus Mecanique

www.sciencedirect.com

2-D hydro-viscoelastic model for convective drying of deformable and unsaturated porous material

Lamine Hassini [a,*], Lamloumi Raja [a], Gisèle Laure Lecompte-Nana [b], Mohamed Afif Elcafsi [a]

[a] University of Tunis El Manar, Faculté des sciences de Tunis, Laboratoire d'énergétique et des transferts thermique et massique (LETTM), Tunisia

[b] Université of Limoges, Laboratoire de science des procédés céramiques et traitements de surface (SPCTS), UMR CNRS 7315, Centre européen de la céramique, 12, rue Atlantis, 87068 Limoges cedex, France

ARTICLE INFO

Article history:
Received 30 October 2016
Accepted 16 February 2017
Available online 15 March 2017

Keywords:
Modelling
Unsaturated cellulosic-clay composite
Convective drying
Viscoelastic stress
Cracking risk

ABSTRACT

The aim of this work was to simulate in two dimensions the spatio-temporal evolution of the moisture content, the temperature, the solid (dry matter) concentration, the dry product total porosity, the gas porosity, and the mechanical stress within a deformable and unsaturated product during convective drying. The material under study was an elongated cellulose–clay composite sample with a square section placed in hot air flow. Currently, this innovative composite is used in the processing of boxes devoted to the preservation of heritage and precious objects against fire damage and other degradation (moisture, insects, etc.). A comprehensive and rigorous hydrothermal model had been merged with a dynamic linear viscoelasticity model based on Bishop's effective stress theory, assuming that the stress tensor is the sum of solid, liquid, and gas stresses. The material viscoelastic properties were measured by means of stress relaxation tests for different water contents. The viscoelastic behaviour was described by a generalized Maxwell model whose parameters were correlated to the water content. The equations of our model were solved by means of the 'COMSOL Multiphysics' software. The hydrothermal part of the model was validated by comparison with experimental drying curves obtained in a laboratory hot-air dryer. The simulations of the spatio-temporal distributions of mechanical stress were performed and interpreted in terms of material potential damage. The sample shape was also predicted all over the drying process.

1. Introduction

For a long time, mathematical models have been proposed to describe the heat and mass transfer phenomena within a product subjected to convective drying. Recently, special attention has been paid to the mechanical aspect of drying, in order to address dried product quality issues such as irregular shape, skin cracks, and breaking [1–6].

For granular media drying like ceramic, clay and concrete, many models assumed that such materials can be considered as saturated throughout drying [7,5,8]. However, the hypothesis of a still saturated medium is a strong assumption; most

* Corresponding author. Fax: +216 70860434.
E-mail address: hassini_lamine@yahoo.fr (L. Hassini).

http://dx.doi.org/10.1016/j.crme.2017.02.004
1631-0721/

Nomenclature

List of symbols

a_w	Water activity	
C_{pl}	Specific heat capacity of liquid water	J/kg/K
C_{ps}	Specific heat capacity of solid matter	J/kg/K
D_v^{eq}	Equivalent water vapour diffusivity of the product	m^2/s
$E(t)$	Instantaneous elasticity modulus	MPa
G	Shear modulus	MPa
h	Superficial heat transfer coefficient	$W/m^2/K$
k	Superficial mass transfer coefficient	m/s
K_g^{eq}	Equivalent gas phase permeability of the product	m^2
K_{rg}	Relative permeability of the liquid phase	
K_l^{eq}	Equivalent liquid phase permeability of the product	m^2
K_{rl}	Relative permeability of the gas phase	
M_a	Air molar mass	kg/mol
M_v	Water vapour molar mass	kg/mol
n_l	Liquid flux	kg/m/s
n_s	Solid flux	kg/m/s
P_{atm}	Atmospheric pressure	Pa
P_c	Capillary pressure within the product	Pa
P_g	Total pressure of the gas phase within the product	Pa
P_l	Liquid pressure within the product	Pa
P_v	Water vapour pressure within the product	Pa
P_{vsat}	Saturation pressure of water vapour	Pa
R	Ideal gas constant	J/mol/K
t	Time	s
T	Product temperature	°C, K
T_a	Air temperature	°C
u	Displacement	m
v_a	Air velocity	m/s
v_s	Solid matter velocity	m/s
X	Product water content dry basis	kg/kg

Greek symbols

Δh_{des}	Specific differential enthalpy of water desorption	J/kg
Δh_{vap}	Specific differential enthalpy of water vaporization	J/kg
ϕ	Total porosity of the dry product	
φ	Air relative humidity	%
λ_{eq}	Equivalent thermal conductivity of the product	W/m/K
μ_l	Dynamic viscosity of liquid phase	kg/m/s
ν_l	Kinematic viscosity of the gas water	m^2/s
ν_g	Kinematic viscosity of liquid phase	m^2/s
ρ_l	Liquid water density	kg/m^3
ρ_s	Apparent density of the dry product	kg/m^3
ρ_{ss}	Density of dry solid	kg/m^3
τ	Tortuosity of the dry product	

initially saturated porous matrices will lose moisture to the environment during storage in an unsaturated environment at less than 100% of relative humidity because a gaseous phase is very likely to appear from the end of the isenthalpic drying period. It seems more appropriate to take into account the existence of the gaseous phase, especially the fact that it plays a main role in the appearance of cracks.

Concerning specifically the mechanical strain and stress within the product during drying, many models considered a purely elastic behaviour [7,3,9]. However, an elasticity hypothesis is not acceptable for products that have the capacity to store and dissipate mechanical energy. Viscoelasticity is much more appropriate to predict correctly the deformation in many ceramics and building materials subjected to drying [8,4,10,11]. The generalized Maxwell model has commonly been used to express viscoelastic properties [10,12,13]. In most works dealing with this model, the parameters of the relaxation function were considered constant. But this approximation is often not satisfactory because the mechanical properties of a water-rich material depend strongly on the water content.

The first author of this study has already a large contribution to two recent publications. The first one was based on the results of simulations predicted by a 2-D viscoelastic model applied to the hot-air drying of a long saturated potato sample with viscoelastic properties [14]. The second one was based on simulation results predicted by a 2-D hydrothermal model applied to the hot-air and microwaves drying of unsaturated agglomerated sand. The model developed in the latter paper was used to predict the internal gas pressure and binder distribution inside the material [6].

This article continues our works on the modelling of physical phenomena within deformable materials during drying processes. Its objective was to propose a set of 2-D transitory equations describing the hydrothermomechanical state of a deformable and unsaturated product during hot-air drying. The originality of this hydrothermomechanical model resides in part in the strong hydromechanical coupling generated by Bishop's effective stress theory for unsaturated media using saturation as Bishop's parameter [15]. The coupling variables are the solid matter velocity and the fluid pressure in the pores.

A long clay–cellulose fibre composite sample (see Fig. 1) with square section (dimensions: $60 \times 10 \times 10$ mm^3) was chosen as a testing material. This innovative product was obtained after incorporation of plant cellulosic fibres (7%) in a commercial clay mixture. One of its important applications is the processing of boxes devoted to the preservation of heritage and precious objects against fire damage and other degradation (moisture, insects, etc.). During the drying process, the material may undergo some damages, like irregular shape, cracks, or even fractures, which are mainly caused by heterogeneous stresses and deformations. These problems generally occur when the drying operating conditions are not well scheduled. The physical drying model proposed here can be thus used particularly as a reliable predictive and optimization tool for the industrial drying of this innovative material.

In order to implement the model, the material transport and equilibrium properties were determined as a function of the state variables (the water content and the temperature). The viscoelastic properties were measured by compressive relaxation tests and were correlated to water content, which was one of the original contributions of this article.

The equations of our model were solved numerically by means of the 'COMSOL Multiphysics' finite-elements software using both the open 'PDE coefficient form' mode and the structural mechanics modules and moving mesh application mode. The hydrothermal part of the model was validated on the basis of the experimental average water content curves for drying trials at different operating conditions. The drying tunnel (designed and constructed in the LETTM Laboratory) was of a vertical type with full control of the drying air. The spatiotemporal evolution of the moisture content, the temperature, the solid (dry matter) concentration, the dry product total porosity, the gas porosity, and the mechanical stress within the material during drying were predicted. The temporal evolution of mechanical stress at different specific points of the sample were simulated and interpreted in terms of the cracking risk of the material. In addition, the sample's shape at the moment when a fracture risk occurs was also predicted.

2. Modelling

2.1. Assumptions

- The material is multiphase and heterogeneous at the microscopic scale, but is represented by an equivalent homogeneous medium with continuously varying state variables and macroscopically defined properties.
- The different phases are in local thermodynamic equilibrium as concerns temperature and vapour pressure.
- The liquid phase flows by filtration due to the gas phase pressure gradient by capillarity due to the liquid water content gradient and by advection due to shrinkage.
- The heat is transferred by conduction and advection associated with the liquid and solid phase flows.
- The vapour moves by filtration due to the gas phase pressure gradient, by thermodiffusion due to the temperature gradient, by ordinary diffusion due to the water content gradient and by advection due to shrinkage.
- The shrinkage is ideal and isotropic.
- The material behaves according to Maxwell's model of viscoelasticity with infinitesimal strain.
- The deformation was plane over the (x, y) plane.

2.2. Internal transfer model

The internal heat and mass transfer model was based on our recently published modelling work with application to agglomerated sand assumed undeformable and submitted to hot air and microwave drying [6]. The equations of the model will not be presented here in details because of the limited space allocated to this article.

The full equation system of the model consists of five PDEs: the solid mass balance equation determining the solid (dry matter) concentration (ρ_s), the heat transfer equation determining the temperature (T), the liquid water transfer equation determining the liquid water content (X), the dry air transfer equation determining the gas pressure (P_g), and the water vapour transfer equation determining the mass of liquid water vaporized per unit volume (m_{vap}). The advective terms due to shrinkage were written using the solid matter velocity. This velocity was determined by solving simultaneously the mechanical part of the model. It should be noted that the solid matter velocity (v_s), the liquid pressure ($P_l = P_g - P_c$) and the gas pressure (P_g) constitute the coupling variables between the hydrothermal and mechanical equations.

In order to reduce the length of these equations, the numerous physical parameters representing the medium properties of the material were grouped into global coefficients m and k. The full set of equations describing the solid, water and heat transfer within the product will be as follows:

Solid transfer

$$\frac{\partial \rho_s}{\partial t} = -\operatorname{div}(\rho_s \vec{v}_s) \tag{1}$$

Heat transfer

$$m_{11}\frac{\partial T}{\partial t} + m_{14}\frac{\partial m_{vap}}{\partial t} = \operatorname{div}(k_{11}\operatorname{grad} T) - n_l C_{pl}\operatorname{grad} T - n_s C_{ps}\operatorname{grad} T \tag{2}$$

where n_l and n_s are the liquid and solid fluxes, respectively given by:

$$n_s = \rho_s \vec{v}_s \tag{3}$$

$$n_l = \rho_s X \vec{v}_s - \frac{K_l^{eq}}{\nu_l}\operatorname{grad} P_g + \frac{K_l^{eq}}{\nu_l}\frac{\partial P_c}{\partial X}\operatorname{grad} X \tag{4}$$

Liquid water transfer

$$m_{22}\frac{\partial X}{\partial t} = \operatorname{div}(\alpha_v \vec{v}_s + k_{21}\operatorname{grad} T + k_{22}\operatorname{grad} X + k_{23}\operatorname{grad} P_g) - \rho_s \vec{v}_s \operatorname{grad} X \tag{5}$$

$$\alpha_v = \frac{M_v P_v}{RT}\left(\phi - X\frac{\rho_s}{\rho_l}\right) \tag{6}$$

Dry air transfer

$$m_{31}\frac{\partial c_s}{\partial t} + m_{32}\frac{\partial T}{\partial t} + m_{33}\frac{\partial X}{\partial t} + m_{34}\frac{\partial P_g}{\partial t} = \operatorname{div}(\alpha_a \vec{v}_s + k_{31}\operatorname{grad} T + k_{32}\operatorname{grad} X + k_{33}\operatorname{grad} P_g) \tag{7}$$

$$\alpha_a = \frac{M_a(P_g - P_v)}{RT}\left(\phi - X\frac{\rho_s}{\rho_l}\right) \tag{8}$$

Water vapour transfer

$$m_{44}\frac{\partial m_{vap}}{\partial t} = \operatorname{div}(\alpha_v \vec{v}_s + k_{41}\operatorname{grad} T + k_{42}\operatorname{grad} X + k_{43}\operatorname{grad} P_g) \tag{9}$$

The exact expressions of the m (capacities) and k (conductances) coefficients pertaining to the above five transfer equations are given in Appendix A. The term $\partial m_{vap}/\partial t$ in Eqs. (2) and (9) represents the liquid-to-vapour phase change rate term. This term is not the accumulation term for vapour mass. The accumulation of vapour mass in a control volume was neglected.

Eqs. (2), (5), (7) and (9) are not only coupled by the gradients of the state variables (X, T, and P_g) and the solid velocity (v_s), but also by the m and k coefficients. These coefficients are in fact combinations of the product's properties (material density, thermal conductivity, fluid permeabilities, species diffusivities) that depend on state variables. The semi-empirical expressions describing these properties have to be known with some precision and to be consistent with each other in order to obtain realistic results without numerical problems.

It is also interesting to note that in the equation (7) the coefficients m depend on the total porosity of the dry product ϕ (also called dry product total porosity in the literature). Since the material shrinks during drying, its porosity ϕ, which is equal to the sum of the gas' (ϕ_g) and the liquid's (ϕ_l) porosities, changes continuously. Porosity can be determined at any instant by conserving the mass of the solid phase, which does not change during the drying process:

$$\rho_{ss} V(X)(1-\phi) = \rho_{ss} V_o (1-\phi_o) \tag{10}$$

where V is the wet sample's volume and V_o is the initial sample's one:

$$\phi = 1 - \frac{(1-\phi_o)}{(V/V_o)} \tag{11}$$

In this formula, $V(X)/V_o$ is the relative volume, depending on material moisture content, determined experimentally.

2.3. Structural mechanical model

The mechanical model consisted mainly of the mechanical equilibrium equation (Eq. (12)), written as follows:

$$\nabla(\sigma_{ij}) = 0 \tag{12}$$

Following Bishop's effective stress approach for unsaturated media [15], the stress tensor σ_{ij} is the sum of the solid, liquid and gas stresses. Coussy and Dangla [16] and Gray and Schrefler [17] proposed the following formula:

$$\sigma_{ij} = \sigma_{ij,s} - SP_l - (1-S)P_g \tag{13}$$

where S is saturation, expressed as:

$$S = \frac{X}{X_{sat}} \tag{14}$$

and

$$X_{sat} = \phi\frac{\rho_l}{\rho_s} \tag{15}$$

Concerning the viscoelastic behaviour, $\sigma_{ij,s}$ (effective solid stress) is given by the expression (16), developed by Rao et al. [18] and used in several previous works. In our case, the parameters of the viscoelastic material depend on time and the water content:

$$\sigma_{ij,s}(t) = \int_0^t \left(K(t-\tau) - \frac{2}{3}G(t-\tau)\right)\frac{\partial \varepsilon_{kk}(\tau)}{\partial \tau}\delta_{ij}\mathrm{d}\tau + 2\int_0^t G(t-\tau)\frac{\partial \varepsilon_{ij}(\tau)}{\partial \tau}\mathrm{d}\tau \tag{16}$$

G and K are shear and bulk moduli, respectively, determined from the following expressions:

$$G(t) = E(t)/3(1-2\nu) \tag{17}$$

and

$$K(t) = E(t)/2(1+\nu) \tag{18}$$

$E(t)$ is the relaxation function also called the instantaneous Young modulus, determined experimentally, and ν is Poisson's ratio.

In numerical solid mechanics, these equations are solved in terms of displacement (u) in the x and y directions. The relations between the elements of the total strain tensor, displacements, and solid matter velocity with the assumption of a small deformation are given below:

$$\varepsilon_{ij} = \frac{1}{2}\left(\frac{\partial u_i}{\partial x_j} + \frac{\partial u_j}{\partial x_i}\right) \tag{19}$$

$$v_s^i = \frac{\partial u_i}{\partial t} \tag{20}$$

where u_i is the displacement of a material point ($i = x,\ y$).

The solid matter's velocity can be calculated from the solid phase conservation equation (Eq. (1)).

2.4. Initial and boundary conditions

- The sample was initially at uniform temperature, water content and gas pressure (atmospheric pressure), and was stress free.

$$X = X_o; \qquad T = T_o; \qquad \sigma_{ij} = 0 \tag{21}$$

- The heat and water transfer at the sample surface in contact with the air was supposed to be purely convective; then the gas pressure at the product surface is equal to the atmospheric pressure:

$$(n_l + n_v)|_{surf} = k\frac{P_{atm}M_v}{RT_a}\ln\left(\frac{P_{atm} - \varphi P_{vsat}(T_a)}{P_{atm} - a_w(X,T)P_{vsat}(T)}\right) \tag{22}$$

$$\lambda_{eq}\frac{\partial T}{\partial n}|_{surf} + \Delta h_{vap} n_l|_{surf} = h(T_a - T_{surf}) \tag{23}$$

$$P_g^{surf} = P_{atm} \tag{24}$$

where $a_w = \frac{-(B-X)^2+[(B-X)^2-4AC]^{0.5}}{2A}$ if $(X \le X_{sat})$ else $a_w = 1$, calculated from Dent's model describing the desorption isotherms of the material (see Table 1).

- At any point of the sample's external surface, the stress that is normal to that surface is zero,

$$\sigma_{ii}^{surf} = 0 \tag{25}$$

- The heat and mass transfer and the solid displacement in the y (vertical) direction at the surface in contact with the shelf ($y = 0$) were considered nil:

$$\frac{\partial X}{\partial y} = 0; \qquad \frac{\partial T}{\partial y} = 0; \qquad u_y = 0 \tag{26}$$

- The heat and mass transfer and the solid displacement in the x (horizontal) direction at the symmetry plane ($x = 0$) were considered nil:

$$\frac{\partial X}{\partial x} = 0; \qquad \frac{\partial T}{\partial x} = 0; \qquad u_x = 0 \tag{27}$$

2.5. Model implementation

The coupled heat and mass transfer equations, and the mechanical equilibrium equations, along with the viscoelastic rheological behaviour law, were solved simultaneously on a variable geometrical domain. In that way, the actual deformation of the sample respecting the global equilibrium and boundary constraints, and not an arbitrary one, was applied to solve the heat and mass balances.

Because of the symmetry of the problem (see Fig. 1), the model equations were solved on a two-dimensional domain, spanning over the half (5 mm × 10 mm) of a cross-section of the cellulose–clay composite sample. The governing equations as well as initial and boundary conditions were numerically implemented by means of the COMSOL Multiphysics

Table 1
Values and expressions of material properties and external heat and mass transfer coefficients used in the simulations.

Material property	Value or correlation	
Initial total porosity of the dry product	$\phi_o = 0.37$	
Initial tortuosity of the dry product	$\tau_o = 2$	
Specific permeability of the product	$K_o = 10^{-13}$ m^2	
Apparent density of the dry product	$\rho_{ss} = 2330$ (kg/m^3)	
Apparent density of the liquid phase	$\rho_l = 1000$ (kg/m^3)	
Equivalent specific heat capacity of the product	$C_{ps} = 1050$ (J/kg/K) at 80 °C and $C_{ps} = 950$ (J/kg/K) at 60 °C	
Relative permeability of the liquid phase	$K_{rl} = S^{\gamma}(1-(1-S^{1/m})^m)^2$	$n = 5.2$ $m = 1 - 1/n$ $g = 9.81$ m s^{-2} $\alpha = 0.029$ $\gamma = 0.25$ $S = X/X_{sat}$
Relative permeability of the gas phase	$K_{rg} = (1-S)^{\gamma}(1-(1-S^{1/m})^m)^{2m}$	
Capillary pressure in the product	$P_c = (\rho_l g/\alpha)(S^{-1/m}-1)^{1/n}$ (P_a)	
Equivalent conductivity of the product	$\lambda_{eq} = 0.3258\ln(X) + 1.8439$ (W/m/K)	
Equilibrium moisture content (Dent Model)	$X_{eq}(a_w, T) = \frac{a_w}{Aa_w^2+Ba_w+C}$ (kg/kg), A, B and C are fundamental constants	
	T (°C) | A | B | C 60 | −52.6556 | 52.3908 | 3.4588 80 | 34.9179 | −111.598 | 82.9242	
Equivalent water vapour diffusivity of the product	$D_v^{eq} = (\phi_o/\tau_o)K_{rg}D_{va}$ (m^2/s)	
Specific differential enthalpy of water vaporization	$\Delta h_{vap} = 4187[597.3 - 0.592(T-273)]$ (J/kg)	
Specific differential enthalpy of water desorption	$\Delta h_{des} = 67{,}740\exp(-15{,}45X)$ (J/kg)	
Partial pressure of water vapour in the product	$P_v = a_w P_v(P_a)$	
Saturation moisture content	$X_{sat} = \phi_o\ (\rho_l/\rho_s)$ (kg/kg)	
Relaxation elastic modulus and relaxation times	$E(t,X) = E_c + E_1(X)\exp(-t/\tau_1) + E_1(X)\exp(-t/\tau_2)$ (MPa) $E_c(X) = 12.5\exp(-10.1630X)$ $E_1(X) = \frac{1}{(0{,}078+13e^6X^{21.33})}$ $E_2(X) = \frac{1}{(0.035+941{,}4X^{9.32})}$ $\tau_1 = 50$ s and $\tau_2 = 5000$ s	
Convective heat transfer coefficient	$h = 0.180\frac{\lambda_a}{d}(\frac{v_a d\rho_a}{\mu_a})^{0.699}Pr^{0.35}$ (W/m^2/K)	
Convective mass transfer coefficient	$k = h/(\rho_a C_{pa} Le^{2/3})$ (m/s) (Le: Lewis number; for typical air–water systems, $Le \approx 1$)	

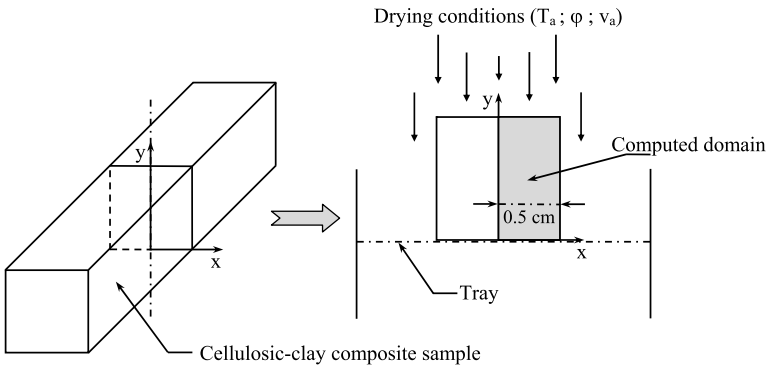

Fig. 1. The sample orientation in the drying tunnel and in the computational domain.

finite-element software using both the 'Chemical Engineering' and the 'Structural mechanics' modules and moving mesh application mode. The computational mesh mapping the solution domain was defined by means of triangular elements.

The values or expressions (functions of X and T) for all material thermophysical and viscoelastic properties and external heat and mass transfer coefficients (h and k) needed for simulations are given in Table 1. In this study, the main thermophysical and viscoelastic properties (heat conductivity λ, heat capacity of the solid matter C_{ps}, water activity a_w obtained from desorption isotherms, enthalpy of water desorption Δh_{des}, dry product total porosity ϕ_o, density of the dry solid ρ_{ss}, instantaneous elasticity modulus $E(t)$) were determined experimentally [19]. The hydraulic product properties (capillary suction, liquid permeability) and the gas phase transport properties (gas permeability, vapour pressure, and diffusivity) were adapted from the literature to the case of similar materials [20,21]. The convective heat transfer coefficient h was taken

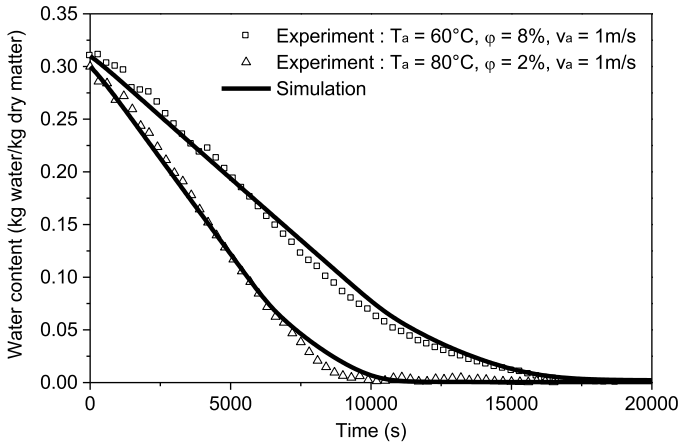

Fig. 2. Average water content of the product versus time for different drying conditions.

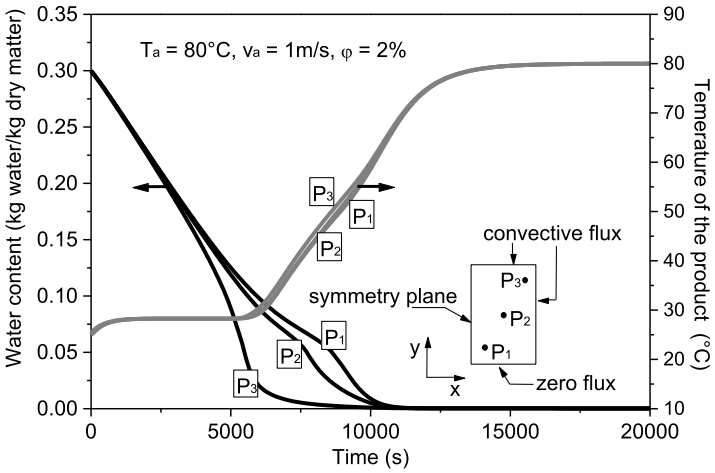

Fig. 3. Simulated distributions of water content and temperature.

from Incropera and Dewitt [22], while the convective mass transfer coefficient k was determined using Chilton–Colburn's analogy [23].

3. Simulation results

3.1. Hydrothermal state simulation

The experimental and simulated temporal-evolution of the cellulosic-clay composite sample mean moisture content is shown in Fig. 2. There was a reasonably good agreement between the experimental and simulated results. For all drying conditions, the mean relative (or percentage) error (MRE) for our data was around 7%, while 10% is generally considered as the worst acceptable value. The slight misfit observed could be attributed, on the one hand, to measurement errors (especially in the mass record due to the support vibration generated by the airflow), and on the other one to the simplifying hypothesis of the model (especially that of linear isotropic shrinkage and linear viscoelastic behaviour).

The simulated temperature and water content distributions inside the sample for different drying conditions are presented in Fig. 3. According to our results, the sample temperature profile exhibited a plateau at a value corresponding to the wet-bulb temperature of the hot air, and thus there existed a constant drying rate phase in the considered process. The temperature inside the sample was practically uniform during the falling rate period. This can be explained by the small size of the sample, the higher thermal conductivity of the product (found at above 1.2 W/m/K for moisture contents above 0.15 kg/kg) and rather gentle hot-air temperature. This means that the water gradient-driven transfer mechanisms (filtration due to the gas phase pressure gradient, capillarity due to the liquid water content gradient and advection due to shrinkage) were certainly the limiting phenomena for water removal. This was the reason for a non-uniform distribution of the moisture content in the sample [7], which generated internal stress and that will be analysed in the next section.

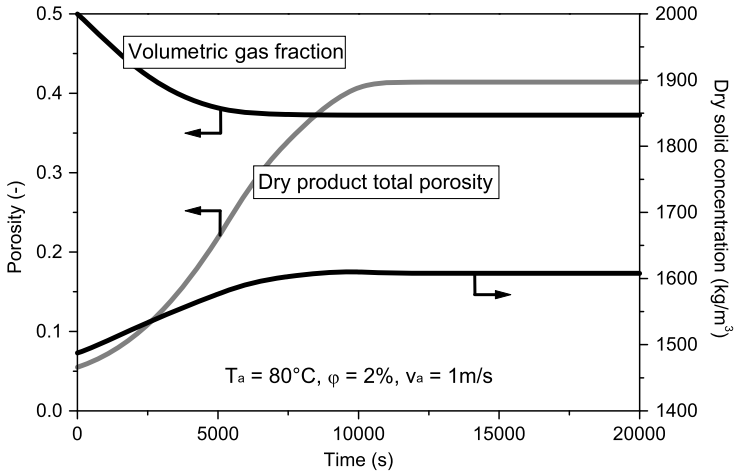

Fig. 4. Average dry solid density, dry product total porosity and volumetric gas fraction versus time.

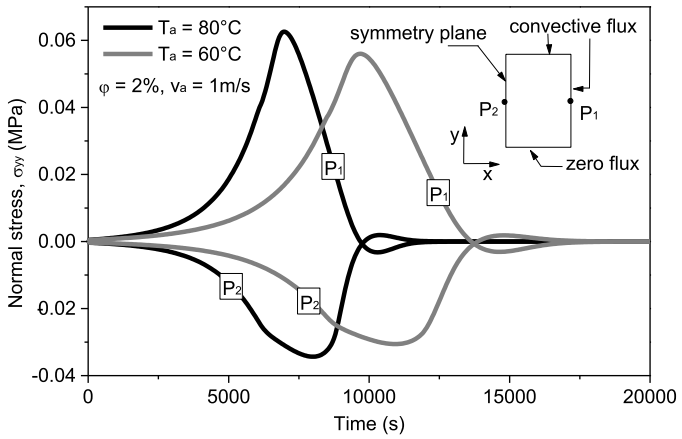

Fig. 5. Stress in the y direction versus time at different drying temperatures.

According to Fig. 4, one can easily observe that due to the shrinkage of the sample during drying, the average dry solid density, the dry product total porosity, and the volumetric gas fraction are not constant during the drying process. These parameters undergo a significant variation and reach a constant value at the end of the drying when the material becomes rigid.

3.2. Mechanical state simulation

The evolution of the normal stress in the y direction (σ_{yy}) with time at a point situated at the lateral surface and a point in the core of the sample for different drying temperatures is depicted in Fig. 5.

These profiles, like all the other ones presented in this section, are calculated in the (x, y) plane in the middle length of the sample. Conventionally, the positive and negative values of the stress correspond to the tensile and compressive stresses, respectively. One can observe that locally the stress changed its sign during the drying course. This phenomenon of stress reversal is specific to a viscoelastic (also plastic) behaviour, as observed by different authors [1,2,9,4,14]. One can also observe in Fig. 5 that the cracking risk was stronger for a sample dried at a higher temperature. For the stronger operating drying condition (drying with hot air at 80 °C), the eventual damage of the sample may occur after about 2 h of drying, when the tensile stress passed by a maximum. This moment corresponds roughly to the beginning of the falling rate period (see Fig. 3). It was very close to the value of 1.85 h found by Kowalski et al. [24] for a saturated cylindrical Kaolin sample ($r = 0.03$ m, $h = 0.06$ m) dried convectively at 150 °C using a viscoelastic model. However, in the case of a parallelepipedic sample of clay material, with approximate dimensions of $1.5 \times 12 \times 15$ cm^3 considered partially saturated, elastic and dried convectively at 40 °C, Chemkhi et al. [9] found that the normal stresses reached their maximum after 40 min of drying. According to Musielak [7], the normal stresses of clay plate of thickness 5 cm and dried convectively at temperature of 60 °C and at a relative humidity of 80% reach their maximum at almost 20 h of drying. In this study, the material was supposed saturated with water and brittle-elastic.

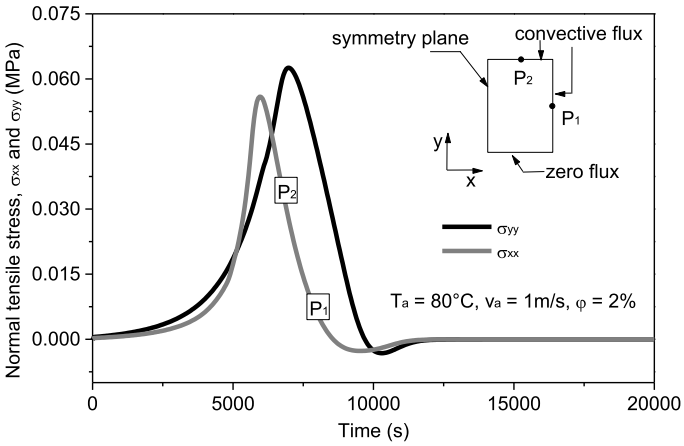

Fig. 6. Tensile stress in the y and x directions versus time.

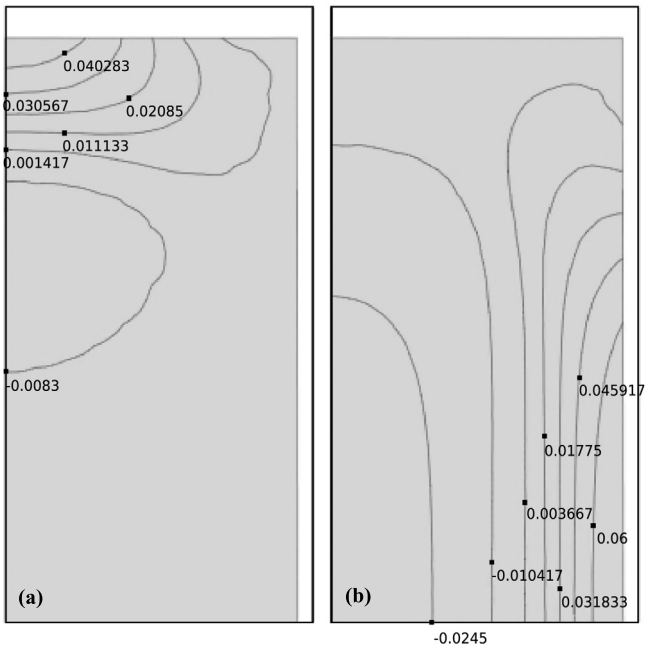

Fig. 7. Normal stress distribution (a, σ_{xx}, b, σ_{yy}) and sample contour at 2 h of drying ($T_a = 80\,^{\circ}C$, $v_a = 1$ m/s, $\varphi = 2\%$).

According to Fig. 6, the maximum tensile stress was located on the sample surface in contact with air. At the beginning of drying, the x-directed (horizontally) normal stress on the top surface was the strongest, but later on and until the end of drying, the y directed (vertically) normal stress on the lateral surface was the strongest. This was due to the high hydric shrinkage in the superficial layer and indicated that the risk of cracking caused by volume shrinkage affected mainly the lateral surface. However, these cracks, if they existed, could not expand into the inner part of the sample because it was in compression.

The simulated samples' contours and the normal stress (σ_{yy} and σ_{xx}) distribution are shown in Fig. 7. The external rectangular frame of the plots represents the initial (before drying) sample contour, while the internal curved frame represents the current sample contour. It can be seen that the maximum tensile stress was located on the sample surface in contact with air, which is consistent with the results previously shown. The simulated sample shape after 2 h of drying is practically rectangular and similar to the original one. This deformation behaviour justifies its use as a precious material in ceramics industries, in particular in the technology of boxes devoted to the preservation of heritage objects. Chemhi et al. [9] and Hammouda and Mihoubi [25] simulated the sample shape of rectangular saturated clay during drying, respectively by an elastic and viscoelastic mechanical model; and the same deformation behaviour of the sample was found.

4. Conclusion

A relevant internal, two-dimensional drying model coupling all heat and water transfer mechanisms (filtration, capillarity, advection) and structural mechanics has been developed. The particularity of this drying model results in its structural mechanical part, which is based on the Bishop's effective stress theory using saturation as the Bishop parameter. The coupling variables with the internal transfer model are solid matter velocity and fluid pressure. The model equations were numerically implemented using the COMSOL Multiphysics finite-elements solver. It was applied to the convective drying of deformable, unsaturated, and viscoelastic material. The test case was an innovative material (clay–cellulose fibre composite) dried convectively by hot air in a vertical tunnel.

The hydrothermal part of the model was validated by comparison with experimental drying curves obtained in a laboratory hot-air dryer. The model was then used to foresee the spatiotemporal evolution of the moisture content, the temperature, the solid (dry matter) concentration, the dry product total porosity, the gas porosity, and the mechanical stress within the material. The average dry solid density, the dry product total porosity, and the volumetric gas fraction changed during the drying process and reached constant values at the end of the drying when the material becomes rigid. A stress reversal phenomenon due to the viscous effect was exhibited. In addition, a cracking risk at the external lateral surface of the sample was demonstrated. The model is also able to predict the sample shape during the process.

This comprehensive and rigorous hydrothermomechanical model can be used as a reliable predictive and optimisation tool for industrial high-temperature drying processes involving unsaturated innovative granular materials undergoing substantial shrinkage and intense water vaporization.

Appendix A

The coefficients of the model presented in this paper are given below:

$$m_{11} = (\rho_s C_{ps} + \rho_l C_{pl})$$

$$m_{14} = \Delta h_{vap}(T) + \Delta h_{des}(X)$$

$$m_{22} = \rho_s$$

$$m_{31} = -\frac{M_a}{RT}\frac{X}{\rho_l}(P_g - P_v)$$

$$m_{32} = -\frac{M_a}{RT}\left(\phi - X\frac{\rho_s}{\rho_l}\right)\left[\frac{\partial P_v}{\partial T} + \frac{(P_g - P_v)}{T}\right]$$

$$m_{33} = \frac{M_a}{RT}\left[\left(\frac{\partial \phi}{\partial X} - \frac{\rho_s}{\rho_l}\right)(P_g - P_v) - \frac{\partial P_v}{\partial X}\left(\phi - X\frac{\rho_s}{\rho_l}\right)\right]$$

$$m_{34} = \frac{M_a}{RT}\left(\phi - X\frac{\rho_s}{\rho_l}\right)$$

$$m_{44} = 1, \qquad k_{11} = \lambda_{eq}$$

$$k_{21} = \frac{M_v P_v}{RT}\left(1 - \frac{P_v(M_v - M_a)}{M_v P_v + M_a(P_g - P_v)}\right)\frac{\partial P_v}{\partial T}$$

$$k_{22} = \frac{M_v P_v}{RT}\left(1 - \frac{P_v(M_v - M_a)}{M_v P_v + M_a(P_g - P_v)}\right)\frac{\partial P_v}{\partial X} - \frac{K_l^{eq}}{\nu_l}\frac{\partial P_c}{\partial X}$$

$$k_{23} = \frac{M_v P_v}{M_v P_v + M_a(P_g - P_v)}\frac{K_g^{eq}}{\nu_g} - \frac{M_v D_v^{eq}}{RT}\frac{P_v M_a}{M_v P_v + M_a(P_g - P_v)} + \frac{K_l^{eq}}{\nu_l}$$

$$k_{31} = -\frac{M_v D_v^{eq}}{RT}\left(1 - \frac{P_v(M_v - M_a)}{M_v P_v + M_a(P_g - P_v)}\right)\frac{\partial P_v}{\partial T}$$

$$k_{32} = -\frac{M_v D_v^{eq}}{RT}\left(1 - \frac{P_v(M_v - M_a)}{M_v P_v + M_a(P_g - P_v)}\right)\frac{\partial P_v}{\partial X}$$

$$k_{33} = \frac{M_a(P_g - P_v)}{M_v P_v + M_a(P_g - P_v)}\frac{K_g^{eq}}{\nu_g} + \frac{M_v D_v^{eq}}{RT}\frac{P_v M_a}{M_v P_v + M_a(P_g - P_v)}$$

$$k_{41} = -\frac{M_v D_v^{eq}}{RT}\left(1 - \frac{P_v(M_v - M_a)}{M_v P_v + M_a(P_g - P_v)}\right)\frac{\partial P_v}{\partial T}$$

$$k_{42} = -\frac{M_v D_v^{eq}}{RT}\left(1 - \frac{P_v(M_v - M_a)}{M_v P_v + M_a(P_g - P_v)}\right)\frac{\partial P_v}{\partial X}$$

$$k_{43} = -\frac{M_v P_v}{M_v P_v + M_a(P_g - P_v)} \frac{K_g^{eq}}{\nu_g} + \frac{M_v D_v^{eq}}{RT} \frac{P_v M_a}{M_v P_v + M_a(P_g - P_v)}$$

The parameters P_c, P_v, D_v, K_l, K_g, λ, ν are product-specific functions of state variables X and T.

References

[1] P. Perré, J. Passard, A physical and mathematical model able to predict the stress field in wood over a wide range of drying conditions, Dry. Technol. 22 (1–2) (2004) 27–44.
[2] J. Banaszak, S.J. Kowalski, Theoretical and experimental analysis of stresses and fractures in clay like materials during drying, Chem. Eng. Process. 44 (2005) 497–503.
[3] R. Peczalski, D. Falgon, A. Julien, J.C. Boyer, E. Vidal-Sallé, Impact of density gradients on the stress level within a green ceramic compact during drying, Dry. Technol. 23 (2005) 1–82.
[4] R. Rémond, J. Passard, P. Perré, The effect of temperature and moisture content on the mechanical behaviour of wood: a comprehensive model applied to drying and bending, Eur. J. Mech. A, Solids 26 (2007) 558–572.
[5] S.J. Kowalski, Control of mechanical processes in drying. Theory and experiment, Chem. Eng. Sci. 65 (2010) 890–899.
[6] L. Hassini, R. Peczalski, J.-L. Gelet, Drying of granular medium by hot air and microwaves. Modeling and prediction of internal gas pressure and binder distribution, Powder Technol. 286 (2015) 636–644.
[7] G. Musielak, Possibility of clay damage during drying, Dry. Technol. 19 (8) (2001) 1645–1659.
[8] K. Khalfaoui, S. Chemkhi, F. Zagrouba, Modeling and stress analysis during drying of a deformable and saturated porous medium, Dry. Technol. 31 (10) (2013) 1124–1137.
[9] S. Chemkhi, F. Zagrouba, A. Bellagi, Mathematical model for drying of highly shrinkage media, Dry. Technol. 22 (5) (2004) 1023–1039.
[10] Y. Itaya, S. Taniguchi, M. Hasatani, A numerical study of transient deformation and stress behavior of a clay slab during drying, Dry. Technol. 15 (1) (1997) 1–21.
[11] J. Jiang, J. Lu, R. Huang, X. Li, Effects of time and temperature on the viscoelastic properties of Chinese fir wood, Dry. Technol. 27 (11) (2009) 1229–1234.
[12] Z.X. Gong, A.S. Mujumdar, Y. Itaya, S. Mori, M. Hasatani, Drying of clay and nonclay media: heat and mass transfer and quality aspects, Dry. Technol. 16 (6) (1998) 1119–1152.
[13] A. Léonard, S. Blacher, M. Crine, W. Jomaa, Evolution of mechanical properties and final textural properties of resorcinol-formaldehyde xerogels during ambient air drying, J. Non-Cryst. Solids 354 (10–11) (2008) 831–838.
[14] L. Hassini, R. Peczalski, P. Laurent, S. Azzouz, 2-D hydro-viscoelastic model for convective drying of highly deformable saturated product, Dry. Technol. 33 (2015) 1872–1882.
[15] A.W. Bishop, The principle of effective stress, Tekn. Ukebl. 39 (1959) 859–863.
[16] O. Coussy, P. Dangla, Approche énergétique du comportement des sols non saturés, in: O. Coussy, J.-M. Fleureau (Eds.), Mécanique des sols non saturés, Lavoisier, Paris, 2002, pp. 137–174.
[17] W.G. Gray, B.A. Schrefler, Analysis of the solid phase stress tensor in multiphase porous media, Int. J. Numer. Anal. Methods Geomech. 31 (4) (2007) 541–581.
[18] V.N.M. Rao, D.D. Hamann, J.R. Hammerle, Stress analysis of a viscoelastic sphere subjected to temperature and moisture gradients, J. Agric. Eng. Res. 20 (3) (1975) 283–293.
[19] R. Lamloumi, Comportement des matériaux minéraux de grande diffusion lors du séchageétude expérimentale et modélisation, PhD thesis, Université de Tunis El Manar, Tunisia & Université de Limoges, France, 2007.
[20] P. Salagnac, P. Glouannec, D. Lecharpentier, Numerical modeling of heat and mass transfer in porous medium during combined hot air, infrared and microwaves drying, Int. J. Heat Mass Transf. 47 (2004) 4479–4489.
[21] T. Constant, C. Moyne, P. Perré, Drying with internal heat generation: theoretical aspects and application to microwave heating, AIChE J. 42 (2) (1996) 359–368.
[22] F.D. Incropera, D.P. Dewitt, Fundamentals of Heat and Mass Transfer, 4th ed., John Wiley & Sons, New York, 1996.
[23] J.P. Halmann, Heat Transfer, seventh ed., McGraw–Hill, 1990.
[24] S.J. Kowalski, K. Rajewska, A. Rybicki, Stresses generated during convective and microwave drying, Dry. Technol. 23 (2005) 1875–1893.
[25] I. Hammouda, D. Mihoubi, Modelling of drying induced stress of clay: elastic and viscoelastic behaviours, Mech. Time-Depend. Mater. 18 (1) (2014) 97–111.